

# Néel-type antiferromagnetic order and magnetic field–temperature phase diagram in the spin- $\frac{1}{2}$ rare-earth honeycomb compound $\text{YbCl}_3$

Jie Xing,<sup>1,\*</sup> Erxi Feng,<sup>2,\*</sup> Yaohua Liu,<sup>2</sup> Eve Emmanouilidou,<sup>1</sup> Chaowei Hu,<sup>1</sup> Jinyu Liu,<sup>1</sup> David Graf,<sup>3</sup>  
Arthur P. Ramirez,<sup>4</sup> Gang Chen,<sup>5,6</sup> Huibo Cao,<sup>2,†</sup> and Ni Ni<sup>1,‡</sup>

<sup>1</sup>*Department of Physics and Astronomy and California NanoSystems Institute, University of California, Los Angeles, California 90095, USA*

<sup>2</sup>*Neutron Scattering Division, Oak Ridge National Laboratory, Oak Ridge, Tennessee 37831, USA*

<sup>3</sup>*National High Magnetic Field Laboratory, 1800 E. Paul Dirac Drive, Tallahassee, Florida 32310, USA*

<sup>4</sup>*Department of Physics, University of California, Santa Cruz, California 95064, USA*

<sup>5</sup>*Department of Physics and Center of Theoretical and Computational Physics, The University of Hong Kong, Pokfulam Road, Hong Kong, China*

<sup>6</sup>*State Key Laboratory of Surface Physics and Department of Physics, Fudan University, Shanghai 200433, China*



(Received 6 March 2019; revised 1 June 2020; accepted 12 June 2020; published 17 July 2020)

Most of the searches for Kitaev materials deal with  $4d/5d$  magnets with spin-orbit-coupled  $J = 1/2$  local moments such as iridates and  $\alpha\text{-RuCl}_3$ . Here we propose the monoclinic  $\text{YbCl}_3$  with a  $\text{Yb}^{3+}$  honeycomb lattice for the exploration of Kitaev physics. We perform thermodynamic,  $ac$  susceptibility, angle-dependent magnetic torque, and neutron diffraction measurements on  $\text{YbCl}_3$  single crystal. We find that the  $\text{Yb}^{3+}$  ion exhibits a Kramers doublet ground state that gives rise to an effective spin  $J_{\text{eff}} = 1/2$  local moment. The compound exhibits short-range magnetic order below 1.20 K, followed by a long-range Néel-type antiferromagnetic order at 0.60 K, below which the ordered  $\text{Yb}^{3+}$  spins lie in the  $ac$  plane with an angle of  $16(11)^\circ$  away from the  $a$  axis. These orders can be suppressed by in-plane and out-of-plane magnetic fields at around 6 and 10 T, respectively. Moreover, the Néel temperature varies nonmonotonically under the out-of-plane magnetic fields, suggesting a reduced spin dimensionality. Together with the strong in-plane magnetic anisotropy and the reduced order moment  $0.8(1) \mu_B$  at 0.25 K, all indicate that  $\text{YbCl}_3$  could be a two-dimensional spin system to approximate the Kitaev physics.

DOI: [10.1103/PhysRevB.102.014427](https://doi.org/10.1103/PhysRevB.102.014427)

## I. INTRODUCTION

In recent years, there has been a tremendous effort aimed at finding a material that supports a quantum spin liquid (QSL) ground state [1,2]. QSL state has long-range entangled spins, which prevent the breaking of symmetry down to zero temperature. Recently, A. Kitaev proposed a pairwise anisotropic spin model for QSL ground state on a honeycomb lattice [3], which presents a  $\mathbb{Z}_2$  state with gapless and nodal Majorana fermion excitations and gapped bosonic visons. A material realization of the Kitaev model was suggested to be present in honeycomb iridates  $A_2\text{IrO}_3$  ( $A = \text{Na}, \text{Li}, \text{H}_3\text{Li}, \text{Cu}$ ) and  $\alpha\text{-RuCl}_3$  [4–28]. The spin-orbit coupling of the iridium or ruthenium moments has been proposed to create highly anisotropic spin interactions including the nearest-neighbor Kitaev interaction [29]. Due to the extended nature of  $4d/5d$  orbitals, in  $A_2\text{IrO}_3$  and  $\alpha\text{-RuCl}_3$ , in addition to a nearest-neighbor Kitaev interaction, further neighbor interactions often exist, leading to greater complexity. It has been suggested theoretically, however, that rare-earth magnets, especially Yb-based ones, may provide a more faithful realization of the Kitaev model [30–34].

The rare-earth  $4f$  electrons experience much stronger spin-orbit coupling and are more localized comparing to  $4d/5d$  electrons [30]. The crystal electric field (CEF) enters as a subleading energy scale and splits the spin-orbital coupled  $J$  states, often leading a twofold degenerated ground state, the so-called the effective spin- $1/2$  ( $J_{\text{eff}} = 1/2$ ), which could present the quantum magnetism in the low dimensional structures [35,36]. Due to the strong localization of the  $4f$  electrons, the spin exchange interaction is usually limited to the nearest neighbors. Although the large magnetic moments of rare earth ions can result in strong long range dipole-dipole interaction coupling that exceeds the exchange energy, for  $\text{Yb}^{3+}$  with  $J_{\text{eff}} = 1/2$ , the dipole-dipole interaction can be ignored as proved in other  $\text{Yb}^{3+}$  [37–39]. These properties suggest that Yb-based compounds may be good systems to study the Kitaev model. In this paper, we carry out an experimental study on the rare-earth honeycomb  $\text{YbCl}_3$  and map out the magnetic field-temperature ( $H$ - $T$ ) phase diagram. The  $J_{\text{eff}} = 1/2$  magnet  $\text{YbCl}_3$  exhibits short-range magnetic order (SRO) at 1.20 K and long-range ordered (LRO) Néel-type antiferromagnetic state below 0.60 K and strong in-plane magnetic anisotropy. The observations of SRO and LRO, in-plane magnetic anisotropy, and reduced order moment demonstrate that  $\text{YbCl}_3$  is indeed a quasi-two-dimensional (2D) frustrated honeycomb that may provide a platform for extending the research of the Kitaev physics.

\*These authors contributed equally to this paper.

†Corresponding author: caoh@ornl.gov

‡Corresponding author: nini@physics.ucla.edu

TABLE I. The crystal structure of  $\text{YbCl}_3$  at 300 K. Wkf. column shows the multiplicity and Wyckoff letter of the site.  $U_{eq}$  is defined as one third of the trace of the  $U_{ij}$  matrix that describes the thermal displacement.

YbCl <sub>3</sub> at 300 K monoclinic $C2/m$ , 330 reflections					
$a = 6.730 \text{ \AA}$ $b = 11.5676 \text{ \AA}$ $c = 6.3326 \text{ \AA}$					
$\alpha = 90.00^\circ$ $\beta = 110.69^\circ$ $\gamma = 90.00^\circ$					
$R_F = 0.119$ $wR_F = 0.152$ $R_F = 0.115$ $\chi^2 = 4.80$					
Atom	Wkf.	$x$	$y$	$z$	$U_{eq}$
Cl1	8j	0.2594(6)	0.3204(6)	0.2402(6)	0.014(1)
Cl2	4i	0.216(1)	0	0.2477(9)	0.013(2)
Yb	4g	0	0.1675(7)	0	0.011(1)

## II. EXPERIMENTAL METHODS

Millimeter-sized transparent  $\text{YbCl}_3$  single crystals with shiny as-grown flat  $ab$  surfaces were grown by the modified Bridgeman method. Commercial  $\text{YbCl}_3$  powder (Alfa Aesar 99.99%) was sealed in a quartz tube under the vacuum and quickly heated up to  $800^\circ\text{C}$ . The ampoule was kept at  $800^\circ\text{C}$  for 10 hours and then cooled to  $500^\circ\text{C}$  at a rate of  $10^\circ\text{C/h}$ . The crystals are soft and can be cleaved easily due to its quasi-2D crystal structure. Magnetic susceptibility and specific heat measurements were performed in a Quantum Design VSM magnetic property measurement system (MPMS3) and physical property measurement system (PPMS), respectively. The crystals decompose into white powder in air (producing  $\text{YbCl}_3 \cdot 6\text{H}_2\text{O}$ ) within a few minutes, therefore, all sample handling was performed inside a glovebox filled with Ar gas. Covering the sample with a thin layer of N grease can prevent it from decomposing in air for hours. During our magnetic measurements, we encapsulated the sample inside a nonmagnetic quartz or copper sample can. To avoid the contribution from paramagnetic impurities, the magnetic susceptibility is calculated as  $\chi = \Delta M / \Delta H = (M(4 \text{ T}) - M(1 \text{ T})) / 3$ . During our specific heat measurement, we made sure that the sample was fully covered by the N grease used in the addenda measurement to prevent the sample decomposition and reduce the measurement error. Single crystal neutron diffraction for

$\text{YbCl}_3$  was measured on the four-circle diffractometer (HB-3A) at the high flux isotope reactor (HFIR) at Oak Ridge National Laboratory (ORNL) [40].

## III. EXPERIMENTAL RESULTS

### A. Crystal structure of $\text{YbCl}_3$

A good fit to the experimental data suggests the sample is of high quality. The refined crystallographic data are summarized in Table I. The compound crystallizes in the monoclinic  $C2/m$  space group, the same as  $\alpha\text{-RuCl}_3$  [18]. The slightly distorted edge-sharing  $\text{YbCl}_6$  octahedra form layered honeycomb  $ab$  planes, as shown in Fig. 1(a). The out-of-plane nearest neighbor distance of  $\text{Yb}^{3+}$  is  $6.3326 \text{ \AA}$  and the in-plane nearest neighbor distance is  $3.90(1) \text{ \AA}$  with the ratio of them being 1.62, slightly less than 1.75 found in  $\alpha\text{-RuCl}_3$  [18].

### B. 2D honeycomb with $J_{\text{eff}} = 1/2$ ground state

Magnetic specific heat is a powerful tool to identify the ground state since it provides the entropy release related to possible phase transitions. The specific heat of  $\text{YbCl}_3$  and isostructural nonmagnetic  $\text{LuCl}_3$  were measured at zero magnetic field, as shown in Fig. 1(b). As insulators, their specific heat data can be written as  $C^{\text{YbCl}_3} = C_{ph}^{\text{YbCl}_3} + C_M$  and  $C^{\text{LuCl}_3} = C_{ph}^{\text{LuCl}_3}$ , where  $C_{ph}$  is the phonon contribution and  $C_M$  is the magnetic contribution. Since both compounds have similar molar mass and crystal structure,  $C_{ph}^{\text{YbCl}_3} = C_{ph}^{\text{LuCl}_3}$  to an accuracy of  $< 1\%$ . Therefore, we can isolate the magnetic contribution of  $\text{YbCl}_3$  by subtracting the lattice part of  $\text{LuCl}_3$  to obtain  $C_M$  by  $C_M = C^{\text{YbCl}_3} - C^{\text{LuCl}_3}$ , as shown in Fig. 1(c). Upon cooling, unlike  $\alpha\text{-RuCl}_3$  which shows LRO at 7 K via a large lambda anomaly [18], the dominant feature in  $\text{YbCl}_3$  is a large broad peak centered at around  $T_1 = 1.20 \text{ K}$ , followed by a small sharp kink at  $T_2 = 0.60 \text{ K}$  and a subtle feature at  $T_3 = 0.40 \text{ K}$  as shown in the inset of Fig. 1(c). Both  $T_1$  and  $T_2$  show no sample variation while  $T_3$  is sample dependent and may be from defects/impurities/imperfections. In addition, a second broad weak specific heat hump centered at around  $100 \text{ K}$  is discernible, which could be attributed to the Schottky anomaly from the discrete energy levels due to CEF effect.

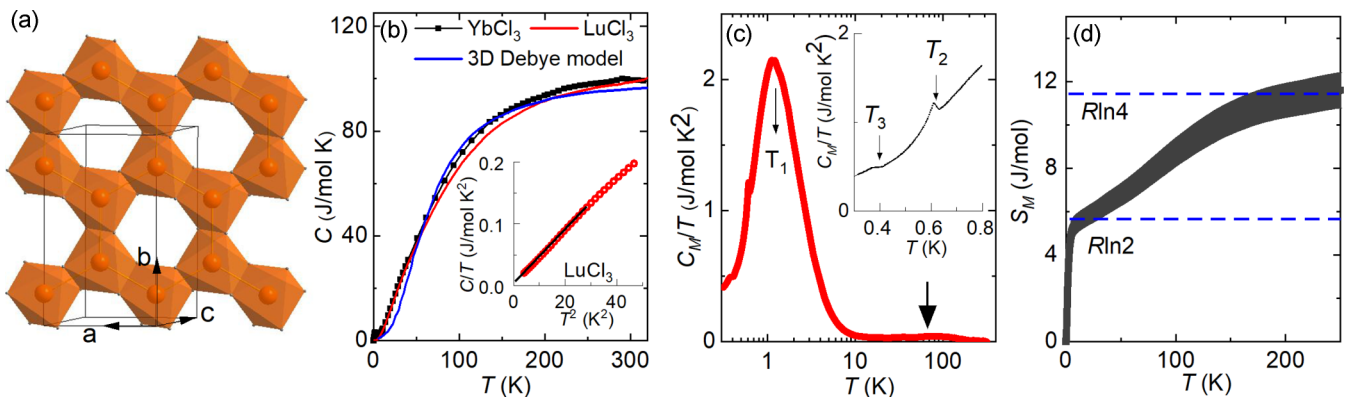


FIG. 1. (a) The crystal structure of the  $ab$  plane of  $\text{YbCl}_3$ . (b) The temperature dependent specific heat  $C$  for  $\text{YbCl}_3$  and  $\text{LuCl}_3$ . The 3D Debye model fitting is shown in blue. Inset:  $C/T$  vs  $T^2$  for  $\text{LuCl}_3$ . (c)  $C_M/T$  vs  $T$  for  $\text{YbCl}_3$ . (d) The temperature dependent magnetic entropy  $S_M$  with error bars.

The magnetic entropy release was calculated based on  $S_m = \int C_M/T dT$  and presented in Fig. 1(d). It provides information on the CEF energy splitting scheme. As a Kramers ion, the state  ${}^2F_{7/2}$  of  $\text{Yb}^{3+}$  would split into four doublets under  $C_2$  symmetry. Upon warming,  $S_m(T)$  exhibits a two-plateau feature, suggesting a substantial CEF energy gap between the ground state and the first excited state.  $S_m(T)$  at the first plateau reaches 5.3(4) J/mol at 8 K, which is very close to  $R \ln 2$  expected for the paramagnetic state of a spin-1/2 system. Around 180 K,  $S_m(T)$  almost saturates at 11.4(8) J/mol, consistent with the full magnetic entropy release  $R \ln(8/2)$  expected from the  $\text{Yb}^{3+}$  ion with doublet ground state [41]. One can estimate the first CEF excited state locating approximately 21 meV, indicating a well isolated ground doublet of  $\text{Yb}^{3+}$  ion at low temperature.

The inset of Fig. 1(b) shows the  $C/T$  vs  $T^2$  plot of  $\text{LuCl}_3$ . By fitting the data from 1.8 K to 6 K with the low temperature limit of 3D Debye model  $C = \beta T^3$ , we obtain the Debye temperature as 260(5) K, a little higher than  $\sim 210$  K of  $\alpha\text{-RuCl}_3$  [15,18]. Although  $C^{\text{LuCl}_3}$  follows the 3D Debye model at low temperatures, large deviations from the model can be seen in Fig. 1(b) at higher temperatures, suggesting the failure of using this 3D model to describe the phonons here. This may not be surprising considering that phonons in  $\alpha\text{-RuCl}_3$  above 15 K can be fitted by 2D Debye model [18].

### C. $H$ - $T$ phase diagram of $\text{YbCl}_3$

To further investigate the nature of the anomalies presented in Fig. 1(c), the magnetic susceptibility and specific heat measurements were performed in a magnetic field. In Fig. 2(a) we show the magnetic susceptibility of  $\text{YbCl}_3$  measured at 1 T above 1.8 K. No LRO is observed above 1.8 K. A Curie-Weiss (CW) fit is made using  $1/\chi = C/(T + \Theta_w)$ , where  $\Theta_w$  is the Weiss temperature and  $C$  is the Curie constant, being related to the effective moment  $\mu_{\text{eff}}$  by  $\mu_{\text{eff}} \approx \sqrt{8C}$ . The fit of the inverse susceptibility from 3 K to 15 K is presented in the inset of Fig. 2(a). The fitted  $\Theta_w^{\parallel} = -6(1)$  K,  $\Theta_w^{\perp} = -9(1)$  K,  $\mu_{\text{eff}}^{\parallel} = 3.1(1) \mu_B/\text{Yb}^{3+}$ , and  $\mu_{\text{eff}}^{\perp} = 3.0(1) \mu_B/\text{Yb}^{3+}$ . The negative  $\Theta_w$  values imply the antiferromagnetic in-plane and out-of-plane exchange interactions. The  $\Theta_w^{\parallel}$  and  $\Theta_w^{\perp}$  are very different, which indicates anisotropic spin interaction as expected for magnetic exchange interaction between  $\text{Yb}^{3+}$  ions. The inferred  $\mu_{\text{eff}}$  is much smaller than  $4.54 \mu_B$  of a free  $J = 7/2 \text{ Yb}^{3+}$  spin, since the  $\text{Yb}^{3+}$  ions should behave like spin-1/2 ions below 20 K due to the well isolated Kramers doublet ground state. Then one can extract the  $g$  factors of in-plane  $g^{\parallel} = 3.6(1)$  and out-of-plane  $g^{\perp} = 3.5(1)$  by using  $\mu_{\text{eff}} = g[J_{\text{eff}}(J_{\text{eff}} + 1)]^{1/2}$  and  $J_{\text{eff}} = 1/2$ .

Figure 2(b) shows the isothermal magnetization up to 7 T. No spontaneous magnetism is observed, again consistent with dominant antiferromagnetic interactions.  $M(H)^{\parallel}$  shows a slope change around 6 T but remains linear for  $M(H)^{\perp}$  up to 7 T. At 7 T, the value of magnetic moment is  $1.7 \mu_B/\text{Yb}^{3+}$  with  $H \parallel ab$  and  $1.1 \mu_B/\text{Yb}^{3+}$  with  $H \perp ab$ , resulting in  $M_{\parallel}/M_{\perp} \sim 1.5$  at 7 T.

Field-dependent  $ac$  susceptibility with  $H \parallel ab$  and  $H \perp ab$  were measured and shown in Figs. 2(c) and 2(d). In both

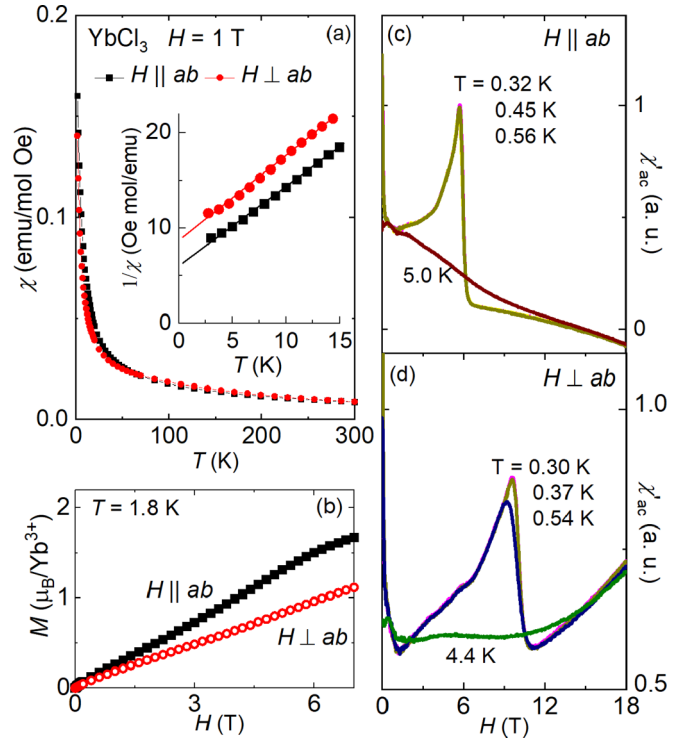


FIG. 2. (a) The temperature dependent magnetic susceptibility of  $\text{YbCl}_3$  at  $H = 1$  T with  $H \parallel ab$  and  $H \perp ab$ . Inset: the inverse magnetic susceptibility  $1/\chi$  from 3 K to 15 K for  $H \parallel ab$  and  $H \perp ab$ . (b) The isothermal magnetization data taken at 1.8 K with  $H \parallel ab$  and  $H \perp ab$ . (c),(d) The field dependent  $ac$  susceptibility  $\chi'_{ac}$  with  $H \parallel ab$  (c) and  $H \perp ab$  (d) at various temperatures. We used a frequency of 577 Hz and current of 0.5 mA.

directions, a cusp feature is seen at moderate fields, suggesting sharp slope change in  $M(H)$ . For  $H \parallel ab$ , the feature occurs at around 5.7 T for temperatures below 0.6 K while for  $H \perp ab$ , it appears at around 9.5 T for temperatures below 0.6 K. Combined with the specific heat data under fields [Fig. 3(a)], we will see that the cusp feature is associated with the suppression of LRO and these two fields are near to the critical fields where the LRO is fully suppressed.

In Fig. 3(a) we plot the temperature dependent  $C/T$  at various magnetic fields. At zero field, the broad hump centered at  $T_1$  releases 99.8% of the ground state entropy, leaving only 0.2% for the tiny sharp peak at  $T_2$ , which is almost 100 orders of magnitude smaller than the entropy release of LRO in  $\alpha\text{-RuCl}_3$  [42]. With increasing fields, the entropy release is suppressed for the transition at  $T_1$  but enhanced for the transition at  $T_2$ . This is a behavior frequently seen under fields for materials with both SRO and LRO, suggesting that the broad hump at  $T_1$  is associated with the SRO and the sharp peak at  $T_2$  signals LRO. Furthermore, an unusual response of  $T_2$  to the applied field is observed, as shown in Fig. 3(a). Instead of being monotonically suppressed by field,  $T_2$  first increases from 0.60 K at 0 T to 0.85 K at 3 T and then gets smoothly suppressed down to 0.50 K at 9 T. This behavior contradicts the mean-field theory which suggests negative  $\partial T_N/\partial H$  with field. But rather it can be understood when theoretical treatment beyond the mean-field theory is employed which has shown

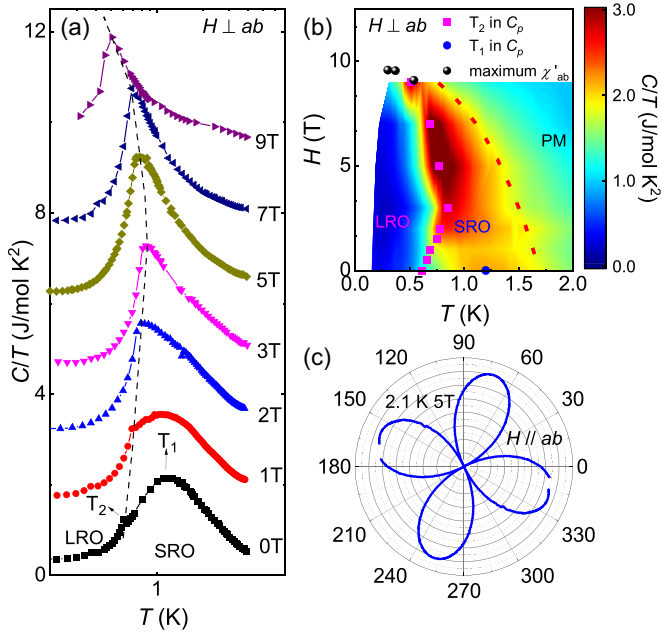


FIG. 3. (a)  $C/T$  vs  $T$  at various magnetic fields. Each data set was offset by 1.5 J/mol K<sup>2</sup>. The dashed line is a guide to the eyes to track the evolution of the SRO features shown in  $C_p$  under field. (b) The  $H$ - $T$  phase diagram of  $\text{YbCl}_3$ . (c) The polar plot of angle-dependent magnetic torque at  $T = 2.1$  K and  $H = 5$  T when the field rotates in the  $ab$  plane. The zero-degree-crystal axis  $l$  was arbitrarily chosen.

that the reduction of spin dimensionality can induce a positive  $\partial T_N/\partial H$  [43]. The reduction of spin dimensionality is a small effect leading to a 0.1% increase of Néel temperature in 3D magnet but is larger with reduced dimensionality. Recently, very similar behavior has been discovered in the entangled 1D spin chain material,  $\text{K}_2\text{PbCu}(\text{NO}_2)_6$ , where  $\partial T_N/\partial H$  changes from positive to negative with increasing field and a broad specific heat hump associated with SRO is observed at higher temperatures [44]. The reduction of spin dimensionality is suggested to explain the sign change and the broad specific heat hump in  $\text{K}_2\text{PbCu}(\text{NO}_2)_6$ . Therefore, this assures that the broad hump at  $T_2$  is associated with the SRO and the sharp peak at  $T_1$  signals LRO in  $\text{YbCl}_3$ . More importantly, the sign change of  $\partial T_N/\partial H$  was observed in a honeycomb material, indicating that  $\text{YbCl}_3$  is the most 2D honeycomb system until now.

Based on our results in Fig. 2(d) and Fig. 3(a), we establish a  $H$ - $T$  phase diagram for  $\text{YbCl}_3$  with  $H \perp ab$  using the contour plot, as presented in Fig. 3(b). At 0.60 K, the sample develops LRO. By applying  $H \perp ab$ , the magnetic field reduces the spin dimensionality, which manifests in the nonmonotonic change of  $T_2$  with the field. The LRO is expected to be fully suppressed at around 10 T with  $H \perp ab$  and at a lower field around 6 T with  $H \parallel ab$  as suggested by Fig. 2(c). On the other hand,  $\text{YbCl}_3$  shows SRO centered around  $T_1 = 1.20$  K at zero field. As shown in this contour plot, it is clear to see that the SRO feature moves to lower temperature with increasing field. The dashed line is used to provide a rough guideline to separate the SRO and PM phases

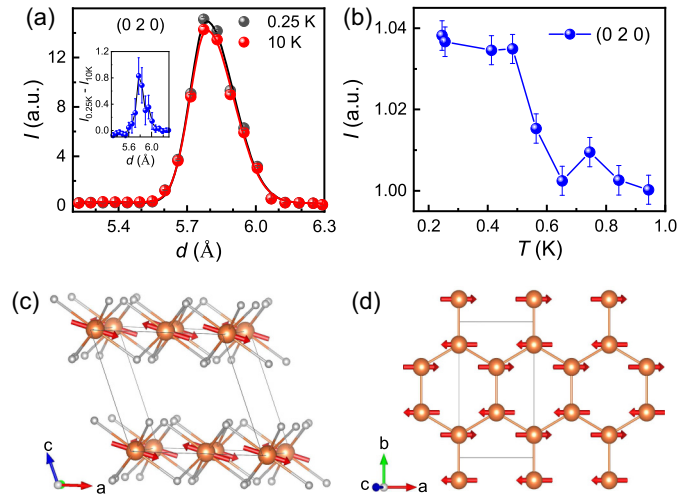


FIG. 4. (a)  $d$  scan of the peak (0 2 0) in the monoclinic setting at 0.25 K and 10 K. The inset shows the difference between 10 K and 0.25 K. (b) Temperature dependence of the integrated intensity of the peak (0 2 0). (c),(d) Néel-type antiferromagnetic structure of  $\text{Yb}^{3+}$  at 0.25 K, the ordered  $\text{Yb}^{3+}$  spins lie in the  $ac$  plane with the angle between the moment and the  $a$  axis as  $16(11)^\circ$ , nearly parallel to the honeycomb  $ab$  plane.

since the PM-SRO is a gradual process of building up the spin-spin correlation.

#### D. Néel-type magnetic structure

Single-crystal neutron-diffraction data were collected at  $T = 0.25$  K and  $T = 10$  K on Corelli at SNS (Spallation Neutron Source) at ORNL. No additional Bragg peaks occur at 0.25 K. However, by subtracting the data at 10 K from that at 0.25 K, the difference reveals the sharp magnetic peaks at the nuclear Bragg positions, indicating the magnetic long-range order with a propagation vector of  $k = 0$ . The magnetic signal on the top of Bragg peaks (0 2 0) [Fig. 4(a)] was measured at various temperatures. As shown in Fig. 4(b), upon cooling, the intensity of the (0 2 0) peak starts to increase at 0.6 K, indicating that LRO emerges below  $T_N = 0.6$  K, consistent with our specific heat results. The magnetic symmetry analysis using MAXMAGN program was employed to solve the magnetic structure [45]. Figures 4(c) and 4(d) present the long-range ordered magnetic structure in  $\text{YbCl}_3$  determined by single crystal neutron diffraction at 0.25 K. The parent space group  $C2/m$  with the  $k$  vector allows four possible maximal magnetic space groups. The  $C2/m$  (#12.60), corresponding to the Néel-type antiferromagnetic order in which the spins lie in the  $ac$  plane and are stacked in parallel along  $c$ , is the only one that fits the observed magnetic peaks. The angle between the ordered moment and  $a$  axis is  $16(11)^\circ$ , making the spins tilt toward the  $ab$  plane. This magnetic structure supports the  $M(H)$  data plotted in Fig. 2(b), which indicates the ordered spins enter the forced ferromagnetic state at a lower field with  $H \parallel ab$ . The refinement of the obtained magnetic peaks gives rise to the ordered  $\text{Yb}^{3+}$  magnetic moment of  $0.8(1) \mu_B$  in the  $ac$  plane. This value is around one third of the fully-ordered moment of  $2.24 \mu_B/\text{Yb}^{3+}$  expected

TABLE II. Magnetic space group (MGS) and the allowed magnetic reflections. • and - represent the allowed and forbidden magnetic reflections in the corresponding magnetic space group, respectively.

Magnetic reflections	Observation	$C2'/m'$ (12.62) FM order in the $a$ - $c$ plane	$C2/m'$ (12.61) Néel type along the $b$ axis	$C2'/m$ (12.60) Néel-type in the $a$ - $c$ plane	$C2/m$ (12.58) FM order along the $b$ axis
(0 0 1)	-	•	-	-	•
(0 2 0)	•	•	-	•	-
(1 1 0)	•	•	•	•	•

from the CEF ground doublet [46], implying strong quantum fluctuation exists at 0.25 K.

### E. Anisotropic in-plane bond-dependent coupling

Since the Kitaev model describes a spin 1/2 honeycomb lattice with highly anisotropic couplings between nearest neighbors, to obtain some information of the nearest neighbor coupling, we investigated the in-plane magnetic anisotropy by measuring the angular dependence of the magnetic torque on the  $\text{YbCl}_3$  single crystal with  $H \parallel ab$  using a cantilever. The data taken at 2.1 K and 5 T are depicted in Fig. 3.  $\theta$  is the angle between  $H$  and the arbitrarily chosen crystal axis  $l$  in the  $ab$

plane. The magnetic torque is very sensitive to the anisotropy of the in-plane magnetization [20,21]. For the  $\text{Yb}^{3+}$  ion, a large portion of the local moment comes from the orbital degrees of freedom. Because the orbitals have orientation, the spin-orbit-coupled local moment would inherit the orbital orientation, and thus the interaction between the local moment would have a strong orientation dependence (or equivalently, bond orientation dependence) [47]. Similar to the pyrochlore magnet  $\text{Yb}_2\text{Ti}_2\text{O}_7$  [37,38], the strong spin-orbital entanglement in the honeycomb magnet  $\text{YbCl}_3$  brings the strong bond dependent interaction. The bond dependent interaction can be determined by the lattice symmetry (or space group symmetry) and is a reflection of the lattice symmetry. For instance, the fourfold symmetry in the magnetic torque was observed in  $\alpha\text{-RuCl}_3$  above or below the zig-zag LRO, suggesting the bond dependent exchange interactions [20,21]. As shown in Fig. 3(c), this bond dependent anisotropy is readily manifested in the magnetic torque measurement. Under magnetic field, the magnetic torque indeed shows fourfold symmetry which agrees with the monoclinic structure and implies the existence of the bond-dependent exchange interactions in  $\text{YbCl}_3$ .

## IV. DISCUSSION

We have established that the ground state of layered  $\text{YbCl}_3$  has a 2D honeycomb spin lattice of  $J_{\text{eff}} = 1/2 \text{ Yb}^{3+}$  spins and revealed the Néel-type magnetic structure with reduced moment and anisotropic in-plane bond-dependent coupling, satisfying the prerequisites of the Kitaev model. The Néel-type antiferromagnetic order with reduced moments makes  $\text{YbCl}_3$  honeycomb distinct from the well-studied  $4d/5d$  honeycomb lattice  $\text{Na}_2\text{IrO}_3$  [8] and  $\text{RuCl}_3$  [16,18,25] hosting the zigzag magnetic order. In the phase diagram of the nearest-neighbor Heisenberg-Kitaev model [48], the honeycomb lattice exhibits a zigzag magnetic order in the region with the ferromagnetic Heisenberg interaction and a Néel-type order for antiferromagnetic Heisenberg interaction. Referring to the phase diagram of the Kitaev-Heisenberg model [49], a magnetic ground state in  $\text{YbCl}_3$  maybe lies next to the Kitaev spin liquid from the antiferromagnetic Heisenberg side [48]. Further investigations, such as inelastic neutron scattering, are needed to settle down this problem.

## V. CONCLUSION

In conclusion, we propose  $\text{YbCl}_3$  as a 2D Kitaev material candidate with  $J_{\text{eff}} = 1/2$  local moments and strong in-plane magnetic anisotropy. This compound exhibits SRO peak at 1.20 K and LRO below  $T_N = 0.60$  K. The application of

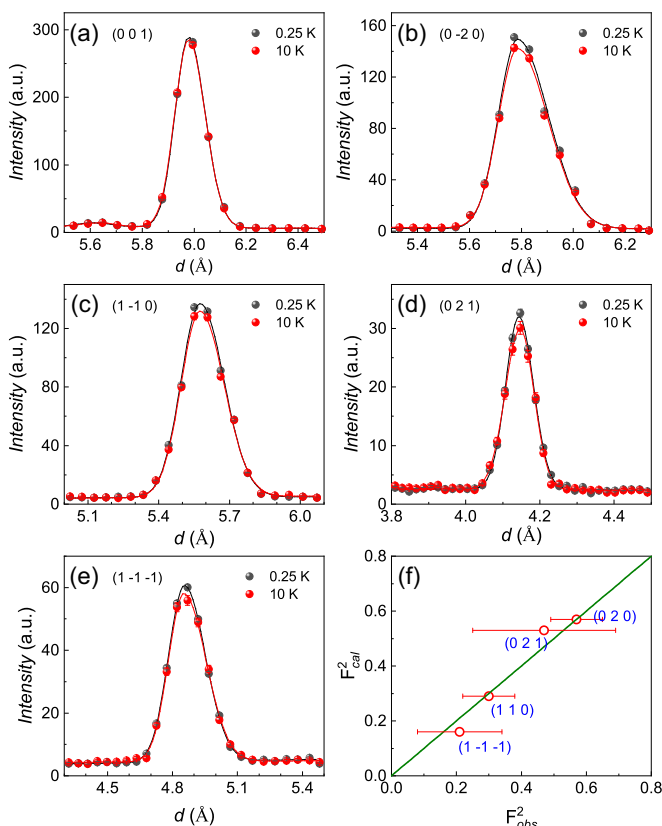


FIG. 5. (a)–(e) The  $d$  scan of the peak (0 0 1), (0 -2 0), (1 -1 0), (0 2 1), and (1 -1 -1) at 0.25 K and 10 K. Most of the error bars are smaller than the size of spheres. The solid line represents the fitting of the peaks by a bi-Gaussian peak function. (f) Comparison of the squared magnetic structure factors between observations and calculations. The magnetic intensities have been normalized to their nuclear intensities.

external magnetic fields can suppress these orders at around 6 T (in-plane field) and 10 T (out-of-plane field). The in-plane magnetic anisotropy and the Néel-type magnetic order with reduced order moment  $0.8(1) \mu_B$  at 0.25 K suggest that  $\text{YbCl}_3$  could be a 2D honeycomb to proximate the Kitaev physics.

#### ACKNOWLEDGMENTS

N.N. thanks Prof. Jeffrey G. Rau for the inspiration to work on this material. Work at UCLA was supported by NSF DMREF program under the award NSF DMREF project DMREF-1629457. Work at UCSC was supported by DOE Grant No. DE-SC0017862. Work at ORNL was supported by U.S. DOE BES Early Career Award No. KC0402010 under Contract No. DE-AC05-00OR22725 and used resources at the Spallation Neutron Source and the High Flux Isotope Reactor, DOE Office of Science User Facilities operated by the Oak Ridge National Laboratory. Work at NHMFL, Tallahassee is supported by NSF through Grant No. NSF/DMR-1644779 and the State of Florida. G.C. acknowledges the support by the Ministry of science and technology of China with Grants No. 2016YFA0301001 and No. 2016YFA0300500.

#### APPENDIX: MAGNETIC SYMMETRY ANALYSIS

Magnetic structure models compatible with the parent space group  $C2/m$  and the propagation vector  $\mathbf{k} = (0, 0, 0)$  are explored using the magnetic symmetry approach using the

MAXMAGN program [45]. There are four possible maximal magnetic space groups as listed in Table II. All four models are collinear magnetic structure and ferromagnetically aligned between hexagonal layers. The moments are either along the  $b$  axis or lying in the  $ac$  plane. Figure 5 presents the  $d$  scan of peak  $(0\ 0\ 1)$ ,  $(0\ 2\ 0)$ ,  $(1\ 1\ 0)$ ,  $(1\ -1\ -1)$ , and  $(0\ 2\ 1)$  at 0.25 K and 10 K. The  $C2'/m'$  (#12.62) and  $C2/m$  are corresponding to the ferromagnetic orders which can be immediately ruled out due to the absence of the magnetic signal at  $(0\ 0\ 1)$ . The  $C2/m'$  (#12.61) is the Néel-type AFM order with magnetic moments along the  $b$  axis, however, the magnetic peak  $(0\ 2\ 0)$  is forbidden in the MSG. Thus, only the  $C2'/m$  (#12.60), which is also Néel-type but moment in the  $ac$  plane, is suitable for our observations.

To refine the magnetic structure in Fullprof suite [50], the self-calibration of the magnetic peak intensity was performed as following:

$$F_{\text{hkl,mag}}^2 = \frac{I_{\text{hkl}}^{0.25\text{ K}} - I_{\text{hkl}}^{10\text{ K}}}{I_{\text{hkl}}^{10\text{ K}}} F_{\text{hkl,nuc}}^2, \quad (\text{A1})$$

where  $I_{\text{hkl}}^{0.25\text{ K}}$  and  $I_{\text{hkl}}^{10\text{ K}}$  are the integrated intensities of peak  $hkl$  at 0.25 K and 10 K, obtained in  $d$  space as shown in Fig. 5.  $F_{\text{hkl,nuc}}^2$  is the squared nuclear structure factor calculated in Fullprof.  $F_{\text{hkl,mag}}^2$  is the self-calibrated magnetic peak intensity. In total 14 peaks (two nuclear and 12 magnetic) were extracted and self-calibrated. Then, they were merged into five nonequivalent reflections and used to refine the magnetic structure in Fullprof.

- 
- [1] P. W. Anderson, *Mater. Res. Bull.* **8**, 153 (1973).  
 [2] F. Mila, *Eur. J. Phys.* **21**, 499 (2000).  
 [3] A. Kitaev, *Ann. Phys. (NY)* **321**, 2 (2006).  
 [4] Y. Singh and P. Gegenwart, *Phys. Rev. B* **82**, 064412 (2010).  
 [5] Y. Singh, S. Manni, J. Reuther, T. Berlijn, R. Thomale, W. Ku, S. Trebst, and P. Gegenwart, *Phys. Rev. Lett.* **108**, 127203 (2012).  
 [6] J. Chaloupka, G. Jackeli, and G. Khaliullin, *Phys. Rev. Lett.* **105**, 027204 (2010).  
 [7] I. I. Mazin, H. O. Jeschke, K. Foyevtsova, R. Valentí, and D. I. Khomskii, *Phys. Rev. Lett.* **109**, 197201 (2012).  
 [8] F. Ye, S. Chi, H. B. Cao, B. C. Chakoumakos, J. A. Fernandez-Baca, R. Custelcean, T. F. Qi, O. B. Korneta, and G. Cao, *Phys. Rev. B* **85**, 180403(R) (2012).  
 [9] J. G. Rau, EricKin-Ho Lee, and H. Y. Kee, *Phys. Rev. Lett.* **112**, 077204 (2014).  
 [10] K. Modic, T. Smidt, I. Kimchi, N. Breznay, A. Biffin, S. Choi, R. Johnson, R. Coldea, P. Watkins-Curry, G. McCandless, J. Chan, F. Gandara, Z. Islam, A. Vishwanath, A. Shekhter, R. McDonald, and J. Analytis, *Nat. Commun.* **5**, 4203 (2014).  
 [11] T. Takayama, A. Kato, R. Dinnebier, J. Nuss, H. Kono, L. S. I. Veiga, G. Fabbri, D. Haskel, and H. Takagi, *Phys. Rev. Lett.* **114**, 077202 (2015).  
 [12] S. Chun, J. Kim, J. Kim, H. Zheng, C. Stoumpos, C. Malliakas, J. Mitchell, K. Mehlawat, Y. Singh, Y. Choi, T. Gog, A. Al-Zein, M. Sala, J. Kirsch, M. Chaloupka, G. Jackeli, G. Khaliullin, and B. J. Kim, *Nat. Phys.* **11**, 462 (2015).  
 [13] K. Kitagawa, T. Takayama, Y. Matsumoto, A. Kato, R. Takano, Y. Kishimoto, S. Bette, R. Dinnebier, G. Jackeli, and H. Takagi, *Nature (London)* **554**, 341 (2018).  
 [14] M. Abramchuk, C. Ozsoy-Keskinbora, J. W. Krizan, K. R. Metz, D. C. Bel, and F. Tafti, *J. Am. Chem. Soc.* **139**, 15371 (2017).  
 [15] A. Banerjee, C. Bridges, J. Yan, A. Aczel, L. Li, M. Stone, G. Granroth, M. Lumsden, Y. Yiu, J. Knolle, S. Bhattacharjee, D. Kovrizhin, R. Moessner, D. Tennant, D. Mandrus, and S. Nagler, *Nat. Mater.* **15**, 733 (2016).  
 [16] C. Titter, *J. Phys.: Conf. Ser.* **746**, 012060 (2016).  
 [17] A. Banerjee, J. Yan, J. Knolle, C. Bridges, M. Stone, M. Lumsden, D. Mandrus, D. Tennant, R. Moessner, and S. Nagler, *Science* **356**, 1055 (2017).  
 [18] H. B. Cao, A. Banerjee, J. Q. Yan, C. A. Bridges, M. D. Lumsden, D. G. Mandrus, D. A. Tennant, B. C. Chakoumakos, and S. E. Nagler, *Phys. Rev. B* **93**, 134423 (2016).  
 [19] K. Ran, J. Wang, W. Wang, Z. Y. Dong, X. Ren, S. Bao, S. Li, Z. Ma, Y. Gan, Y. Zhang, J. T. Park, G. Deng, S. Danilkin, S. L. Yu, J. X. Li, and J. Wen, *Phys. Rev. Lett.* **118**, 107203 (2017).  
 [20] I. A. Leahy, C. A. Pocs, P. E. Siegfried, D. Graf, S. H. Do, K. Y. Choi, B. Normand, and M. Lee, *Phys. Rev. Lett.* **118**, 187203 (2017).  
 [21] P. Lampen-Kelley, S. Rachel, J. Reuther, J.-Q. Yan, A. Banerjee, C. A. Bridges, H. B. Cao, S. E. Nagler, and D. Mandrus, *Phys. Rev. B* **98**, 100403(R) (2018).

- [22] J. A. Sears, M. Songvilay, K. W. Plumb, J. P. Clancy, Y. Qiu, Y. Zhao, D. Parshall, and Y. J. Kim, *Phys. Rev. B* **91**, 144420 (2015).
- [23] K. W. Plumb, J. P. Clancy, L. J. Sandilands, V. V. Shankar, Y. F. Hu, K. S. Burch, H. Y. Kee, and Y. J. Kim, *Phys. Rev. B* **90**, 041112(R) (2014).
- [24] M. Majumder, M. Schmidt, H. Rosner, A. A. Tsirlin, H. Yasuoka, and M. Baenitz, *Phys. Rev. B* **91**, 180401(R) (2015).
- [25] R. D. Johnson, S. C. Williams, A. A. Haghighirad, J. Singleton, V. Zapf, P. Manuel, I. I. Mazin, Y. Li, H. O. Jeschke, R. Valenti, and R. Coldea, *Phys. Rev. B* **92**, 235119 (2015).
- [26] S. H. Baek, S. H. Do, K. Y. Choi, Y. S. Kwon, A. U.B. Wolter, S. Nishimoto, J. van den Brink, and B. Buchner, *Phys. Rev. Lett.* **119**, 037201 (2017).
- [27] J. Zheng, K. Ran, T. Li, J. Wang, P. Wang, B. Liu, Z.-X. Liu, B. Normand, J. Wen, and W. Yu, *Phys. Rev. Lett.* **119**, 227208 (2017).
- [28] J. A. Sears, Y. Zhao, Z. Xu, J. W. Lynn, and Y.-J. Kim, *Phys. Rev. B* **95**, 180411(R) (2017).
- [29] G. Jackeli and G. Khaliullin, *Phys. Rev. Lett.* **102**, 017205 (2009).
- [30] F. Y. Li, Y. D. Li, Y. Yu, A. Paramakanti, and G. Chen, *Phys. Rev. B* **95**, 085132 (2017).
- [31] J. G. Rau and M. J. P. Gingras, *Phys. Rev. B* **98**, 054408 (2018).
- [32] S.-H. Jang, R. Sano, Y. Kato, and Y. Motome, *Phys. Rev. B* **99**, 241106(R) (2019).
- [33] Z.-X. Luo and G. Chen, [arXiv:1903.02530](https://arxiv.org/abs/1903.02530).
- [34] K. Morita, M. Kishimoto, and T. Tohyama, *Phys. Rev. B* **98**, 134437 (2018).
- [35] L. S. Wu, S. E. Nikitin, Z. Wang, W. Zhu, C. D. Batista, A. M. Tsvelik, A. M. Samarakoon, D. A. Tennant, M. Brando, L. Vasylechko, M. Frontzek, A. T. Savici, G. Sala, G. Ehlers, A. D. Christianson, M. D. Lumsden, and A. Podlesnyak, *Nat. Commun.* **10**, 698 (2019).
- [36] M. Bordelon, E. Kenney, T. Hogan, L. Posthuma, M. Kavand, Y. Lyu, M. Sherwin, C. Brown, M. J. Graf, L. Balents, and S. D. Wilson, *Nat. Phys.* **15**, 1058 (2019).
- [37] K. A. Ross, L. Savary, B. D. Gaulin, and L. Balents, *Phys. Rev. X* **1**, 021002 (2011).
- [38] H. Cao, A. Gukasov, I. Mirebeau, P. Bonville, C. Decorse, and G. Dhaleane, *Phys. Rev. Lett.* **103**, 056402 (2009).
- [39] Y. Li, G. Chen, W. Tong, L. Pi, J. Liu, Z. Yang, X. Wang, and Q. Zhang, *Phys. Rev. Lett.* **115**, 167203 (2015).
- [40] B. C. Chakoumakos, H. B. Cao, F. Ye, A. D. Stoica, M. Popovici, M. Sundaram, W. Zhou, J. S. Hicks, G. W. Lynn, and R. A. Riedel, *J. Appl. Crystallogr.* **44**, 655 (2011).
- [41] *Properties And Applications of Complex Intermetallics*, edited by Esther Belin-ferré (World Scientific, Singapore, 2009).
- [42] S.-H. Do, S.-Y. Park, J. Yoshitake, J. Nasu, Y. Motome, Y. S. Kwon, D. T. Adroja, D. J. Voneshen, K. Kim, T.-H. Jang, J.-H. Park, K.-Y. Choi and S. Ji, *Nat. Phys.* **13**, 1079 (2017).
- [43] J. P. A. M. Hijmans, K. Kopinga, F. Boersma, and W. J. M. de Jonge, *Phys. Rev. Lett.* **40**, 1108 (1978).
- [44] N. Blanc, J. Trinh, L. Dong, X. Bai, A. A. Aczel, M. Mourigal, L. Balents, T. Siegrist, and A. P. Ramirez, *Nat. Phys.* **14**, 273 (2018).
- [45] J. M. Perez-Mato, S. V. Gallego, E. S. Tasci, L. Elcoro, G. de la Flor, and M. I. Aroyo, *Annu. Rev. Matter. Res.* **45**, 217 (2015).
- [46] G. Sala, M. B. Stone, B. K. Rai, A. F. May, D. S. Parker, G. B. Halasz, Y. Q. Cheng, G. Ehlers, V. O. Garlea, Q. Zhang, M. D. Lumsden, and A. D. Christianson, *Phys. Rev. B* **100**, 180406(R) (2019).
- [47] W. Witczak-Krempa, G. Chen, Y. B. Kim, and L. Balents, *Annu. Rev. Condens. Matter Phys.* **5**, 57 (2014).
- [48] L. Janssen and M. Vojta, *J. Phys.: Condens. Matter* **31**, 423002 (2019).
- [49] J. Chaloupka, G. Jackeli, and G. Khaliullin, *Phys. Rev. Lett.* **110**, 097204 (2013).
- [50] J. Rodríguez-Carvajal, *Physica B: Condens. Matter* **192**, 55 (1993).